ELSEVIER

Journal of Atmospheric and Solar-Terrestrial Physics 68 (2006) 1730–1751

Journal of ATMOSPHERIC AND SOLAR-TERRESTRIAL PHYSICS

www.elsevier.com/locate/jastp

Tropopause to mesopause gravity waves in August: Measurement and modeling

Peter Preusse[a,*], Manfred Ern[a], Stephen D. Eckermann[b], Christopher D. Warner[c], Richard H. Picard[d], Peter Knieling[e], Mac Krebsbach[a], James M. Russell III[f], Martin G. Mlynczak[g], Christopher J. Mertens[g], Martin Riese[a]

[a]*ICG-I, Forschungszentrum Juelich, Juelich, Germany*
[b]*E. O. Hulburt Center for Space Research, Naval Research Laboratory, Washington, DC, USA*
[c]*Centre for Atmospheric Sciences, University of Cambridge, Cambridge, UK*
[d]*Air Force Research Laboratory, Hanscom Air Force Base, Hanscom, MA, USA*
[e]*Department of Physics, Wuppertal University (BUW), Wuppertal, Germany*
[f]*Hampton University, Hampton, VA, USA*
[g]*NASA Langley Research Center, Hampton, VA, USA*

Available online 23 August 2006

Abstract

Global gravity wave (GW) distributions are retrieved from infrared emission limb soundings taken by the CRISTA instrument in August 1997 and by the SABER instrument in August 2003. The investigated altitudes cover the whole middle atmosphere from the tropopause to the mesopause. The data agree semi-quantitatively in their salient features and only small deviations due to the different meteorological conditions in the two years are observed. Of particular interest is the decrease of GW activity at the top of the southern polar vortex and an accompanying shift of GW activity towards the subtropics in the mesosphere. We emulate this feature by two conceptionally different models, the Warner and McIntyre spectral parameterization scheme and the GROGRAT GW ray tracer. Both models indicate that saturation limits and GW breaking are the governing processes in creating this structure. Also, both models can well reproduce the global distributions except for two important points: (1) convectively generated GWs in the northern subtropics are largely underestimated; (2) northern hemisphere high latitude activity is grossly overestimated. These points indicate that GW distribution in general circulation models are not fully realistic. Refined measurements are required to constrain more realistic GW source distributions.

Keywords: Satellite measurements; Stratosphere; Mesosphere; Gravity waves; Ray tracing

1. Introduction

Ever since the first publications of gravity wave (GW) climatologies from satellites (Fetzer and Gille, 1994; Wu and Waters, 1996; Preusse et al., 2000) the question arose which physical processes

*Corresponding author. Tel.: +49 2461 613532; fax: +49 2461 615346.
E-mail address: p.preusse@fz-juelich.de (P. Preusse).

1364-6826/$ - see front matter © 2006 Elsevier Ltd. All rights reserved.
doi:10.1016/j.jastp.2005.10.019

Report Documentation Page

Form Approved
OMB No. 0704-0188

1. REPORT DATE	2. REPORT TYPE	3. DATES COVERED
AUG 2006		**00-00-2006 to 00-00-2006**

4. TITLE AND SUBTITLE	5a. CONTRACT NUMBER
Tropopause to mesopause gravity waves in August: Measurement and modeling	5b. GRANT NUMBER
	5c. PROGRAM ELEMENT NUMBER
6. AUTHOR(S)	5d. PROJECT NUMBER
	5e. TASK NUMBER
	5f. WORK UNIT NUMBER
7. PERFORMING ORGANIZATION NAME(S) AND ADDRESS(ES) **Naval Research Laboratory,E. O. Hulburt Center for Space Research,Washington,DC,20375**	8. PERFORMING ORGANIZATION REPORT NUMBER
9. SPONSORING/MONITORING AGENCY NAME(S) AND ADDRESS(ES)	10. SPONSOR/MONITOR'S ACRONYM(S)
	11. SPONSOR/MONITOR'S REPORT NUMBER(S)

12. DISTRIBUTION/AVAILABILITY STATEMENT
Approved for public release; distribution unlimited

13. SUPPLEMENTARY NOTES

14. ABSTRACT

Global gravity wave (GW) distributions are retrieved from infrared emission limb soundings taken by the CRISTA instrument in August 1997 and by the SABER instrument in August 2003. The investigated altitudes cover the whole middle atmosphere from the tropopause to the mesopause. The data agree semi-quantitatively in their salient features and only small deviations due to the different meteorological conditions in the two years are observed. Of particular interest is the decrease of GW activity at the top of the southern polar vortex and an accompanying shift of GW activity towards the subtropics in the mesosphere. We emulate this feature by two conceptionally different models, the Warner and McIntyre spectral parameterization scheme and the GROGRAT GW ray tracer. Both models indicate that saturation limits and GW breaking are the governing processes in creating this structure. Also, both models can well reproduce the global distributions except for two important points: (1) convectively generated GWs in the northern subtropics are largely underestimated; (2) northern hemisphere high latitude activity is grossly overestimated. These points indicate that GW distribution in general circulation models are not fully realistic. Refined measurements are required to constrain more realistic GW source distributions.

15. SUBJECT TERMS

16. SECURITY CLASSIFICATION OF:			17. LIMITATION OF ABSTRACT	18. NUMBER OF PAGES	19a. NAME OF RESPONSIBLE PERSON
a. REPORT	b. ABSTRACT	c. THIS PAGE			
unclassified	**unclassified**	**unclassified**	**Same as Report (SAR)**	**22**	

were involved when GW variances decreased with altitude (e.g. Wu, 2001). In general, we expect GW amplitudes to grow with altitude as the background density decreases and particularly large activity is observed in regions of strong background winds. Correlations between wind fields and GW activity were discussed, for instance, by Alexander (1998) and Preusse et al. (2002, 2004). On top of such wind jets, however, the GW activity stalls or decreases. Processes involved can be wave breaking, wave reflection, wave dissipation by turbulent and radiative damping, slant wave propagation and visibility effects due to the different sensitivity of the observing instrument for GWs of different vertical wavelengths. For the momentum balance, of course, it makes a large difference which of these effects is governing.

An example of such a GW activity maximum is observed in zonal mean data of the CRISTA-2 flight and in SABER data taken in August 1997 and August 2003, respectively (cf. Section 2). Very high GW activity is correlated with high wind speeds of a stratospheric jet at ~60°S associated with the winter polar vortex. This activity reaches up to about 60 km. At higher altitudes we find high wind speeds and high wave activity in a mid-latitude/subtropical (~40°S) mesospheric jet. Apparently the waves follow the wind maxima from high to mid-latitudes when they propagate upwards. We use two different models, the Warner and McIntyre spectral parameterization scheme (Warner and McIntyre, 1999, 2001) and the GROGRAT GW ray tracer (Marks and Eckermann, 1995; Eckermann and Marks, 1997) to discern the influence of the aforementioned processes on the observed GW distribution. In particular, we aim at a representative composite of spectral wave components to describe the whole middle atmosphere GW global distribution during CRISTA-2 and the corresponding period of the SABER mission on the basis of a homogeneous and isotropic source.

Section 2 introduces the measurements. In Section 3 we summarize a number of previous investigations on which we base the choice of wave components used for a comprehensive GROGRAT simulation which is described in Section 4. Section 5 introduces results from the Warner and McIntyre spectral model and compares them to the measurements and the GROGRAT results. Finally, the results are summarized and discussed in Section 6.

2. Measurements

The analysis of GWs from thermal infrared emission limb soundings is a well-characterized technique, most analyses focusing on the stratosphere. However, two instruments provide high-quality, high spatial resolution temperature measurements also covering the entire mesosphere: the Cryogenic Infrared Spectrometers and Telescopes for the Atmosphere (CRISTA) (Offermann et al., 1999; Riese et al., 1999), a free-flyer from the Space Shuttle, and the Sounding of the Atmosphere using Broadband Emission Radiometry (SABER) (Mlynczak, 1997; Russell, 1999; Yee et al., 2003) instrument on board the Thermosphere–Ionosphere–Mesosphere Energetics and Dynamics (TIMED) satellite.

2.1. Instruments and data analysis technique

We consider temperatures retrieved from infrared thermal limb emissions taken by the CRISTA instrument in August 1997 and by the SABER instrument in August 2003. The mesospheric CRISTA data presented in this paper are retrieved from a 13.9 μm CO_2 band. During the second CRISTA flight this spectral feature was measured by all of CRISTA's three telescopes. In the altitude range of 35–80 km a high precision of 0.5–1.0 K is obtained. The stratospheric analyses are based on the 12.6 μm CO_2 emission used for previous studies (Preusse et al., 2002; Ern et al., 2004). CRISTA flew on a 57° inclination orbit and by continuous yaw maneuvers a latitude range of 72°S to 72°N was covered (Grossmann et al., 2002). For a general description of the CRISTA data processing see Riese et al. (1999). The SABER temperatures are retrieved from the main CO_2 v_2 emission at 15 μm. A new coupled retrieval algorithm evaluates CO_2 densities and temperatures simultaneously from 4.3 and 15 μm emissions and takes non-local thermodynamic equilibrium (NLTE) effects into account (Mertens et al., 2004). NLTE effects start to exert an influence above ~70 km altitude and become increasingly important in the mesopause and lower thermosphere region.

The retrieved temperature data were analyzed using the algorithms described by Preusse et al. (2002). The data were first detrended by a wavenumber 0–6 Kalman filter. In order to detrend also from tides, ascending and descending orbit nodes were treated separately to avoid mixing of different

local times (cf. Preusse et al., 2001a). The resulting altitude profiles of temperature residuals were analyzed by a combination of the maximum entropy method (MEM) and harmonic analysis (sinusoidal fit). Finally, we obtain altitude profiles of the two leading wave components. The amplitudes, corresponding vertical wavelengths and phases on the same altitude grid as the original temperature data are obtained (Preusse et al., 2002).

2.2. Global distributions

So inferred GW squared temperature amplitudes from the leading wave component are presented in Fig. 1. Shown are world maps at 25, 40 and 60 km altitude on a 2° latitude and 4° longitude grid. The maps were created using a triangular weight with 1500 km radius, i.e. a point is weighted 1, if it coincides with a grid point, zero, if it is at a distance of 1500 km or larger, and the weight decreases linearly with distance in-between. The grid of the maps is hence an oversampling to the width of the triangular weight. At each altitude the color scale is the same for the two instruments. There are slight differences, but the two episodes indicate the same salient features. The maximum GW variances are found around 60°S and coincide with the high wind speeds in the stratospheric jet associated with the polar winter vortex (Preusse et al., 2003a, 2004; Ern et al., 2004). In particular, at 25 km altitude there is

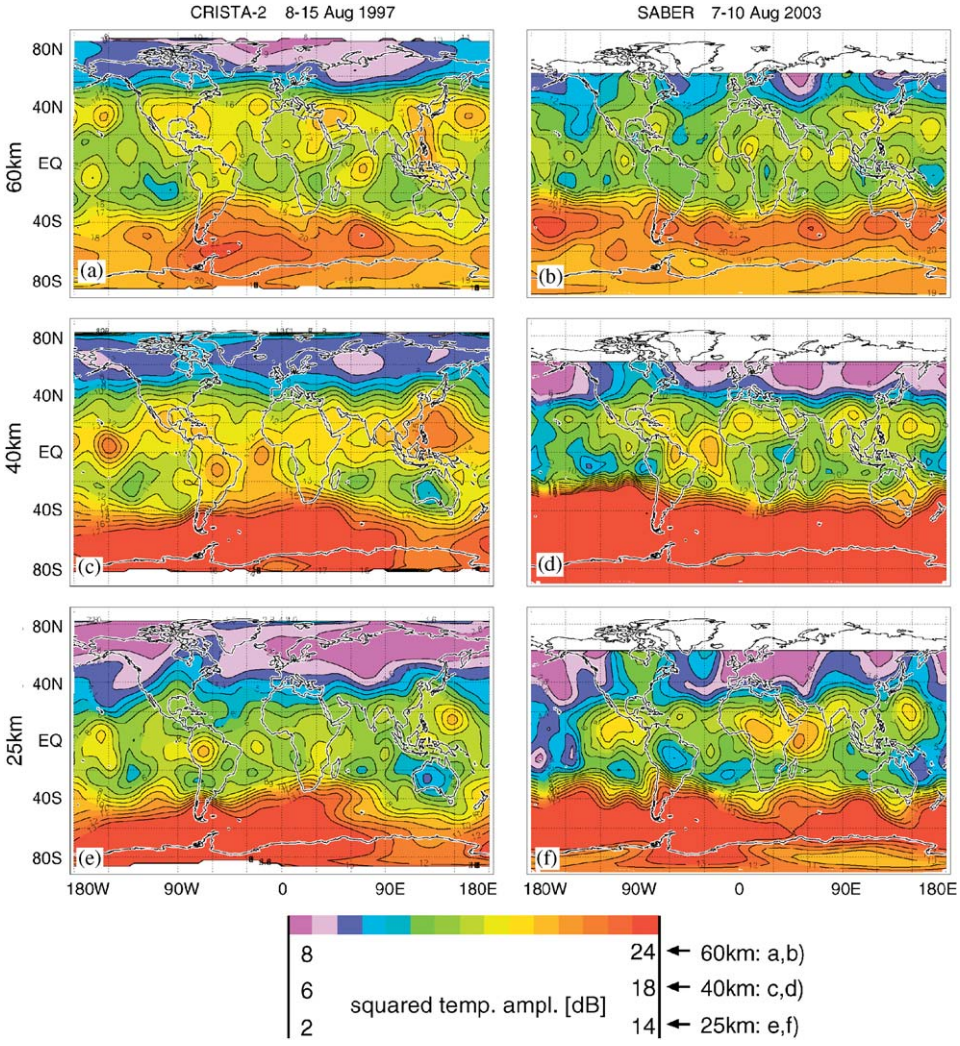

Fig. 1. Comparison of CRISTA and SABER data in world maps of GW-squared temperature amplitudes in dB (reference $1\,K^2$). At individual altitudes the same color scale is used for CRISTA and SABER data. The scaling ranges from 2 to 14 dB at 25 km altitude and increases to 8–24 dB at 60 km altitude.

pronounced activity in the tropics (20°S–20°N). In addition, centers of high wave activity are found in the northern hemisphere (NH) subtropics. The CRISTA data in Fig. 1c,e indicate forcing due to convection above the warm water regions of the Gulf of Mexico and the Kuro-Shio stream (Preusse et al., 2001b; Preusse and Ern, 2005). This feature is less pronounced in the SABER data (Fig. 1d,f). Finally, the high latitudes of the northern (i.e. summer) hemisphere are very quiet. These are all well-known features which are discussed in more detail in Section 3. A peculiarity of the CRISTA-2 data is the strong planetary wave-1/wave-2 activity at high southern latitudes (Riese et al., 2002). These planetary waves map into the GW activity particularly at 60 km altitude. For instance, the GW activity in the longitude interval from 90°W to 90°E is much stronger than the activity in the longitude interval from 90°E to 90°W (or 270°E). It should be emphasized that this is a real enhancement of GW activity and not a problem of the scale separation, i.e. a GW process is required to map the structures of the background wind into the GW variances. At lower altitudes the mapping of the planetary waves is primarily visible by the northward extent of the southern hemisphere (SH) high latitude region of high GW activity. In contrast to CRISTA data, the SABER measurements exhibit very weak longitudinal dependence.

Latitude/altitude cross sections of zonal mean GW squared amplitudes are shown in Fig. 2. In addition, we show CIRA86 (Chandra et al., 1990) zonal mean winds for comparison. The step-like change at 45 km altitude in the CRISTA data indicates the switch-over from the stratospheric data based on the 12.6 μm CO_2 emission to the mesospheric data based on the 13.9 μm emission. The change is emphasized, since both CRISTA data sets were plotted separately and no smoothing algorithm has been applied. For both CRISTA and SABER, the NH subtropical convective belt is visible in GW activity at low altitudes. A general resemblance of the wind fields is observed in the GW squared amplitudes. This phenomenon of a high correlation between wind velocities and GW activity is well known (Alexander, 1998; Preusse et al., 2004) and further discussed in Section 3 and the modeling discussions in Sections 4 and 5. Of particular interest is the altitude region around 60 km. Here, the amplitude growth in the polar vortex ceases and the waves appear to follow the wind speed maximum and turn towards the subtropics. This feature will be discussed in depth in the modeling Sections 4 and 5.

3. Previous work and its relation to the current modeling approach

In this paper we discuss some selected CRISTA and SABER data and we make an attempt to understand these data in terms of GW modeling by using the Warner–McIntyre parametrization and the GROGRAT ray-tracing approach. In particular, for the ray tracing approach there are so many degrees of freedom that one has to rely on an educated guess to compose a suitable distribution of GWs launched at the source level. This educated guess is based on a number of previous studies (our own ones as well as those of other authors and employing a variety of instruments) which are briefly summarized here in order to motivate the assumed launch distributions of the GROGRAT ray tracing studies.

3.1. Visibility filtering

A given instrument or measurement technique is sensitive only to a certain part of the wave spectrum of GWs. There are a number of limiting processes which define the wavelength boundaries, horizontal as well as vertical, of the part of the spectrum visible to a certain instrument. For passive remote sensing techniques the integration along the line of sight and the field of view of the instrument as well as sampling issues are the most important limitations (e.g.; Preusse et al., 2002; Lange and Jacobi, 2003; Jiang et al., 2004a). In addition, GW analyses rely on scale separation, i.e. one has to detrend the data from the background state of the atmosphere including synoptic scale waves. This detrending sometimes also removes a part of the GW spectrum. This imposes for instance a strong vertical visibility filter on radio sonde analyses though the instrument itself is sensitive to waves of all scales. Visibility filtering can control the global distributions observed by an instrument (Alexander, 1998) and even the salient features of the global distribution may change when considered at different wavelengths (Preusse et al., 2000). Visibility filtering is of direct relevance to one of the main features observed in Fig. 2, i.e. the decrease of GW activity on top of the southern polar vortex and the shift to subtropical latitudes. This can be illustrated by a thought experiment. The vertical wavelength λ_z of a GW is given by (mid-frequency approximation,

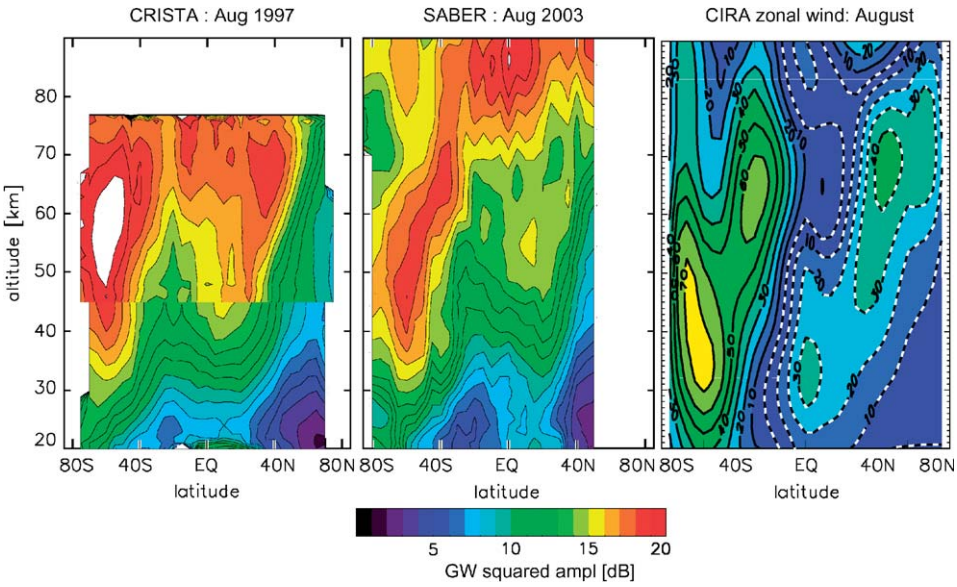

Fig. 2. Comparison of CRISTA and SABER data in zonal means of GW-squared temperature amplitudes (left and middle), as well as with CIRA wind climatology (right). No visibility correction (cf. Preusse et al., 2002) was applied to the SABER data.

cf. Section 2.1.2 of Fritts and Alexander, 2003)

$$\lambda_z = 2\pi \frac{c-u}{N}, \tag{1}$$

with N being the buoyancy frequency, c the horizontal phase speed of the wave, and u the wind velocity in direction of the wave vector. If a GW propagates opposite to the wind, the vertical wavelength becomes larger when the wind speed is higher. Now assume that the main part of the GW variance is found at a low phase speed and that the vertical wavelength of these waves is, without background wind, below the lower limit of the visibility range of the instrument. If these waves now propagate into a wind jet from below, they are refracted to longer vertical wavelengths and become visible, and if they leave the jet at higher altitudes, they become invisible again. In the thought experiment the instrument therefore observes strong activity only in the jet though the real GW activity in the atmosphere has not changed. (See Alexander, 1998, for a more detailed discussion.) To which degree visibility filtering really contributes to the shape of the global distributions presented in Fig. 2 is discussed in Sections 4 and 5.

3.2. Inference of vertical and horizontal wavelength

The vertical wavelength is one of the direct results of the GW analysis algorithm used in this paper (cf. Section 2 and Preusse et al., 2002). Differences in global GW distributions when considered at different vertical wavelengths were analyzed (see previous subsection and Preusse et al., 2000, 2002). However, there is much less known about the dependence on the horizontal wavelength. Horizontal wavelength spectra were inferred from high flying airplanes (Pfister et al., 1993; Bacmeister et al., 1996; Alexander et al., 2000) for specific regions in the lowermost stratosphere covered by aircraft campaigns. At higher altitudes GW spectra were inferred from satellite radiance data (Picard et al., 1998; Eidmann et al., 2001; Wu, 2001). A power law of between $-5/3$ and -2, consistent with theoretical predictions (see Dewan, 1997, and references therein), was found in all these studies though slopes may vary with latitude (Wu, 2001). Due to the flight path or orbit geometry in all these data latitudinal variations mix with spectral characteristics of GWs and a scale separation approach is made to isolate the GW signal. Eidmann et al. (2001) made an attempt to discuss scales longer than 1000 km. However, also in this study the longer scales were judged to be uncertain because of detrending reasons. Hence we have nearly no information on the very long horizontal wavelength GWs and the shape of the spectrum at these scales.

Also, only the MLS-based study (Wu, 2001) made a climatological survey of the geographical dependence of spectral intensity and slope varying

with geographical location. These were averages over three month periods and 20°-wide latitudinal bands. For the interpretation of these results it is important to know that MLS is most sensitive to those waves whose wave fronts are co-aligned with that part of the limb ray where the radiance saturates (McLandress et al., 2000; Jiang et al., 2004a). The sensitivity of MLS to waves of different vertical and horizontal wavelengths (cf. Fig. 12b of McLandress et al., 2000) therefore displays a half-cigar shaped, tilted maximum and the considered horizontal spectra bear an inherent vertical wavelength dependence. In addition MLS is sensitive to comparatively long horizontal wavelength of $\lambda_z > 10$ km. Changes in the slope might therefore be influenced by changes in the vertical wavelength spectrum. One interesting result is that spectra of different altitudes or different latitudes do not cross each other. This means that zonal mean cross sections considered at a specific horizontal wavelength would largely resemble cross sections of a different wavelength. It should be noted, however, that this could be different for specific wave sources.

Some recent information on the average horizontal wavelength of GWs was inferred by Ern et al. (2004) from analyzing the GW phase differences in pairs of adjacent CRISTA profiles. First, profile pairs are selected where the vertical wavelength differs by less than 6 km. This is done in order to remove pairs, that are unlikely to stem from the same wave event. Second, the horizontal wavenumber k is inferred by

$$k = \frac{\Delta\phi}{\Delta x}, \tag{2}$$

where Δx is the distance between the two CRISTA measurements and $\Delta\phi$ is the difference between the two wave phases at a considered altitude. These horizontal wavenumbers are averaged (e.g. in zonal means) and afterwards converted into horizontal wavelengths in order to have a more intuitive number (Ern et al., 2004). In Fig. 3 we show zonal mean horizontal wavenumbers given as horizontal wavelengths for different altitudes as inferred from CRISTA-2 data. The error bars indicate the statistical error of the mean as calculated from the scatter of the wavenumbers. The main uncertainty in the CRISTA data, however, is induced by the sparse horizontal sampling. As shown by Preusse et al. (2002) (cf. brief summary in Section 3.1) waves of horizontal wavelengths longer than $\lambda_h > 100$ km are visible to an infrared limb sounder (200 km along the line of sight, shorter at favorable viewing directions). The profile separation during CRISTA-2 in the stratospheric measuring mode is ~240 km implying a Nyquist wavelength of 480 km. As shown by Ern et al. (2004) the shortest wavelength resulting from an ensemble average is twice the Nyquist wavelength, i.e. 960 km in the CRISTA-2 case (dashed horizontal line in Fig. 3). In addition, the selection of profile pairs favors waves covering a larger area and hence likely biases the average distribution to larger wavelength. The horizontal wavelength distributions reach their maximum at the equator and drop at high latitudes towards the limit caused by the Nyquist wavelength. This

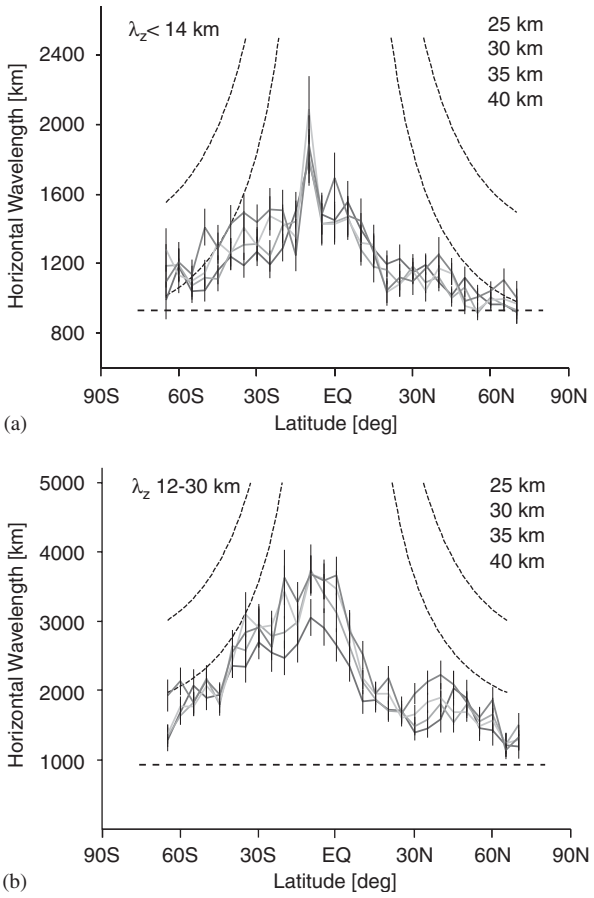

Fig. 3. Zonal mean horizontal wavelength $\bar{\lambda}_h = 2\pi/\bar{k}$ measured by CRISTA-2 (color code gives altitude), horizontal wavelength ensemble average lower limit (horizontal line), and upper limit for two values of constant ω/f (black dashed). The upper panel shows short vertical wavelengths, the lower panel shows long vertical wavelengths. For details see text.

distribution is strongly connected to the equatorial maximum observed in climatologies of short vertical wavelength GWs (Fetzer and Gille, 1994; Tsuda et al., 2000; Preusse et al., 2000).

3.3. The equatorial maximum

The variance maximum observed in short vertical wavelength climatologies of remote sensing (Fetzer and Gille, 1994; Tsuda et al., 2000; Preusse et al., 2000) as well as in situ measurements (Allen and Vincent, 1995) is directly related to the frequency spectrum of GWs as discussed by Alexander et al. (2002). It is generally assumed (Warner and McIntyre, 2001) and also supported by spectral analyses of long duration balloon flights (Hertzog et al., 2002) as well as spectral analyses of horizontal fluctuations (e.g. Bacmeister et al., 1996; Eidmann et al., 2001; Wu, 2001) that the frequency spectrum of GW energy obeys a power law with an exponent of approximately $-5/3$ to -2, i.e. increases at low frequencies. According to the dispersion relation, the minimum frequency (maximum period) of GWs is limited by the Coriolis parameter f. It is, however, most likely that the spectrum does not peak at the limiting lower-bound frequency f, but that the maximum is reached at a frequency slightly larger than f. Assuming that the frequency of this peak is reached at a fixed multiple of f, i.e. that ω/f is constant, and using the average vertical wavelength of the considered waves, we can calculate a maximum or limiting horizontal wavelength by the dispersion relation. Horizontal wavelengths corresponding to $\omega/f = 1.4$ (upper thin black curve) and $\omega/f = 1.8$ (lower curve) are shown in Fig. 3. The $\omega/f = 1.8$ curve limits the shoulders of the measured distributions, except for a dip at 30°N, which we discuss below. This indicates that the Coriolis force limits the horizontal wavelength spectrum. Due to the increase of wave energy at low frequencies an equatorial maximum in wave variance is formed by low-frequency, long horizontal wavelength waves which can only exist at the equator (Alexander et al., 2002). When composing a representative GW spectral distribution for a GROGRAT experiment, we hence have to include waves of very large horizontal wavelengths (several thousand km) and we can launch them homogeneously over the whole globe, since the Coriolis force will do the filtering that is required to produce the equatorial maximum.

3.4. Previous results of spectral GW modeling

In general circulation models (GCMs) spectral parameterization schemes are used to take into account the non-orographic GW drag. Together with orographic GW parameterizations (McFarlane, 1987) they are expected to represent the full wind accelerations imposed by GWs. In August the general background wind conditions filter most of the mountain waves, before these can reach the stratosphere. Only at the southern tip of South-America and at the Antarctic Peninsula do we find both orography and favorable winds allowing mountain waves to propagate into the stratosphere. Distributions measured in August are hence an ideal test case, since the spectral schemes involving only homogeneous isotropic source distributions should describe almost the complete global distribution. In previous studies (Ern et al., 2004, 2005) we compared modeling results of the Warner and McIntyre spectral parameterization scheme (Warner and McIntyre, 1999, 2001) with momentum flux estimates from CRISTA-2 data at 25 km altitude and obtained a very good agreement. The comparison included visibility filtering. The scheme launches GWs isotropically and with a simple latitude dependence (Warner and McIntyre, 2001; Ern et al., 2004), the frequency part of the spectrum is pre-integrated and not considered in the upward propagation. The Warner and McIntyre scheme has several tunable parameters, including the launch level, from which the GW spectrum propagates upward, the vertical wavenumber of maximum momentum at the launch level ($m^\star$) and the spectral slope at long vertical wavelengths (small wavenumbers m). Ern et al. (2004) found strong indication for a low launch level at $\sim$2–5 km altitude. The other tunable parameters were chosen as in the original setup (Warner and McIntyre, 2001; Ern et al., 2004). In a most recent study (Ern et al., 2006) the complete altitude range, for which we can estimate momentum flux, was used to constrain also these tunable parameters. The resulting values are less sharp than for the launch level, but indication was found that the original choice of $m^\star = 2\pi/(2\,\mathrm{km})$ and a slope of $+1$ results in a good agreement. Larger deviations from these values are incompatible with the CRISTA data. Hence, we use in the current study (Section 5) the original choice of parameters and a launch level of $\sim$2.5 km.

The results also motivate us to make an attempt to reproduce the measured distribution by a

GROGRAT experiment based on a homogeneous and isotropic launch distribution. Since we need to investigate the spectral shape and since GROGRAT is computationally much more expensive than the Warner and McIntyre scheme, we launch the GROGRAT waves at 2 km altitude and do not vary this launch altitude (cf. Section 4).

3.5. Convective sources

The Warner and McIntyre modeling of CRISTA-2 data (Ern et al., 2004) underestimates the momentum flux in the NH subtropics. This is likely due to strong GW excitation by convection above the warm water regions of the Kuro-Shio and the Gulf of Mexico as well as convection in the Indian monsoon. A direct link of GW activity to the tropopause altitude and cloudiness was found by Preusse et al. (2001b) in CRISTA data and by Jiang et al. (2004b) in MLS data. A correlation of GW activity with the high sea surface temperature (SST) in the Kuro-Shio and the Gulf of Mexico was found in a one year time series of CLAES data (Preusse and Ern, 2005). In addition, convective forcing is indicated in a narrow equatorial band centered at about 10° latitude in the summer hemisphere (Jiang et al., 2004b; Preusse and Ern, 2005).

These studies of satellite data (Preusse et al., 2001b; Jiang et al., 2004b; Preusse and Ern, 2005) also give hint to properties of these waves. The convectively forced waves have horizontal wavelengths in the range of less than 100 km (Jiang et al., 2004b) to a few 100 km (Preusse et al., 2001b) and they have substantial amplitudes of several K. This is the reason for the dip at NH subtropics in the average horizontal wavelength shown in Fig. 3. The ground-based phase speeds peak around $30\,\mathrm{ms}^{-1}$ and extend to much faster waves also (Preusse et al., 2001b). This spectral composition is corroborated by an apparent northward shift of the convective GW activity centers with altitude observed by MLS (Jiang et al., 2004b), which is only conceivable when visibility filtering of high amplitude, high phase speed waves takes place.

First modeling attempts to parameterize this convective wave forcing on a global scale for incorporation into GCMs exist (Chun et al., 2004; Beres et al., 2005). The approaches reproduce the equatorial band and the locations of the subtropical forcing (Beres et al., 2005). In this paper we do not include explicit convective wave forcing but the existence of such waves is information required for the interpretation of the results.

4. GROGRAT experiments

In the current study we have the primary goal to understand the reason for the decrease of wave activity at the top of stratospheric and mesospheric jets observed in CRISTA-2 and SABER data. Possible reasons for the decrease and equatorward shift of wave activity include instrument visibility, wave breaking and slant wave propagation. In addition, we also aim at constructing a composite launch spectrum, i.e. a composite of a few discrete wave components, which is able to mimic the measured global distributions at all altitudes. It is an interesting goal in itself to test whether the whole GW field can be described by a homogeneous and isotropic launch distribution. Furthermore, only when we understand the whole distribution can we gain confidence that a specific result is valid for the processes in nature and is not an artifact caused by using an unrealistic model setup. Since we have more information from previous investigations on the background atmosphere (Oberheide et al., 2002) as well as the GW distributions (Ern et al., 2004, 2005) for the period of the CRISTA flight than for the SABER August 2003 period, we will focus in our modeling approach on the time period of the CRISTA flight.

The Gravity wave Regional Or Global RAy Tracer (GROGRAT) (Marks and Eckermann, 1995; Eckermann and Marks, 1997) is a tool ideally suited for this study, since it is sufficiently fast to enable global simulations, and since it includes much more aspects of GW physics than the spectral model. The ray tracer follows the trajectory of an upward propagating wave and is hence suited to study slant wave propagation. It is fully rotational and contains also refraction due to the Coriolis force, which is important when considering the equatorial maximum. Finally, it contains wave saturation as well as radiative and dissipative wave damping as well as the possibility to switch off these mechanisms for process studies. For this representation of physical processes we have to pay the price that GROGRAT is an individual-wave model, i.e. that we have no clear concept of the spectral composition of the launch distribution and that we always will undersample this spectral launch distribution. Also, we need to generate our own

procedure to average the individual wave components at a considered location.

4.1. Background winds

Except for the GW properties, the main input to any GW model is the background atmosphere and, in particular, the wind fields. Our attempt to reproduce the observed GW distributions therefore mainly depends on as realistic as possible wind fields. At low altitudes we can rely on ECMWF reanalyses (Coy and Swinbank, 1997). For the CRISTA time period these were limited to 30 km altitude. Newer reanalyses and UKMO data reach up to the stratopause and higher, but since the number of data fed into the assimilation system strongly decreases above 30 km the reliability is much lower than for the troposphere and lower stratosphere. We hence create a composite wind field from ECMWF reanalyses in the troposphere and lower stratosphere (0–28 km), geostrophic wind fields calculated from CRISTA temperatures and pressures (Oberheide et al., 2002) for the stratosphere and mesosphere (20–85 km), and CIRA climatological data Chandra et al. (1990) for the mesopause and the lower thermosphere (70–110 km). At the overlapping altitudes, a smooth transition by a weighted mean was enforced. These data were used for the GROGRAT as well as the Warner and McIntyre modeling experiments. The model results shown extend to 90 km altitude in case of GROGRAT and to 110 km altitude in case of the Warner and McIntyre model. It should hence be kept in mind that at the highest altitudes in the upper mesosphere and the lower thermosphere the winds are based on a climatology with no meridional component and no planetary scale waves included and that tides are neglected. Tidal amplitudes are frequently larger than the background winds at these altitudes (cf. the results of Oberheide et al. (2000) on tidal modeling with the background wind fields (Oberheide et al., 2002; Chandra et al., 1990)). A second limitation of the wind fields is the latitude coverage. We have made no attempt to horizontally expand the CRISTA data and hence the composite winds are restricted by the latitude range of the CRISTA data from 70°S to 70°N.

4.2. Setting up individual spectral components

A GROGRAT ray is initialized by defining the horizontal wave vector, the frequency, the amplitude and the launch position in terms of longitude, latitude and altitude. In this paper we define a single spectral component experiment (SCE) in such a manner that it is nearly a global launch distribution. Rays are launched between 60°S and 60°N at every 5° latitude and between 0° and 360° longitude at every 20° longitude. Rays may leave the 0° to 360° longitude range and are continued cyclically. However, rays are stopped when they cross the latitudinal boundaries of 70°S and 70°N given by the limits of the wind field. At each geographic position rays are launched in eight directions spaced every 45° in azimuth starting from 0°. Motivated by the results of the Warner and McIntyre modeling (Ern et al., 2004, 2005) we launch the rays of all SCEs at 2 km altitude and we use a homogeneous and isotropic launch distribution, i.e. all rays in a specific SCE have the same launch amplitude, which however is changed for other SCEs. An SCE hence consists of 3600 individual rays. The characteristic launch variables of an SCE are the horizontal ground-based phase speed c, the horizontal wavelength λ_h and the amplitude A. We choose to characterize the SCEs rather by phase speed than by frequency, since for waves in the mid-frequency range ($f \ll \omega \ll N$) the propagation characteristics are determined mainly by the phase speed.

A further free parameter, external to GROGRAT, but important when we consider global distributions e.g. in terms of zonal means, is wave intermittency. Whenever we consider maps showing the amplitudes of the individual profiles (Preusse et al., 1999, 2002; Eckermann and Preusse, 1999) or scatter diagrams giving individual values (Preusse et al., 2003a) we often find large differences between adjacent profiles. This is the result of the intermittency of GWs caused by the limited spatial extent and limited lifetime of wave sources. For instance, particularly enhanced GW amplitudes are found directly above the ridge of the Andes and contrast strongly with a low-amplitude background over the ocean (Eckermann and Preusse, 1999). Convective towers initiating mesoscale GWs are estimated to live one to a few hours (Pfister et al., 1993). On the other hand, the satellite always performs a certain number of measurements and, if only a few waves are present, the instrument measures some background wave activity level. When we evaluate an SCE, we therefore need to introduce a background in the simulation which mimics the intermittency of GWs in nature. The probability of waves reaching a certain altitude can

be as important for the shape of a global distribution as the wave amplitudes.

One example is the generation of the equatorial maximum. As described in Section 3.3, very long horizontal wavelength GWs produce this maximum. We therefore run a $c = 30\,\mathrm{ms}^{-1}$, $\lambda_h = 3000\,\mathrm{km}$ SCE. Many rays of this SCE launched at high latitudes are eliminated directly at the launch level for being unphysical. This is shown in the zonal mean altitude–latitude cross sections in Fig. 4. Panel a shows the total number of rays in 5° latitude bands, panel b shows the zonal mean-squared temperature amplitudes, and panel c shows the zonal mean-squared amplitude after introducing a background. At low altitudes the waves are confined to low latitudes. At higher altitudes those waves which propagate opposite to the wind are refracted to higher intrinsic frequencies and can penetrate into higher latitudes, too. In the number of rays we find indication of an equatorial maximum. The squared-amplitude zonal means in panel b show only weak latitudinal dependence and no indication of an equatorial maximum. That there are only few rays at higher latitudes of course has no influence on the amplitudes. To mimic the observed equatorial maximum we therefore add a constant background of 0.5 K temperature amplitudes (i.e. $0.25\,\mathrm{K}^2$ squared temperature amplitudes). This background is kept the same for all altitudes and has the same number of events as the GROGRAT launch distribution. In order to create smoother maps, the multiple events at one location due to the 8 ray directions are redistributed to a finer latitude longitude grid of 2.5° × 5°. After introducing the background we find indication of a low latitude maximum of GW-squared amplitudes in Fig. 4c.

4.3. The importance of saturation for the shape of global distributions

One of the difficulties in generating a suitable launch distribution is that we have to choose a suitable amplitude at the launch level to match the observed amplitudes at much higher altitudes. The amplitude is easily defined when we can assume all waves in an SCE to be saturated already at the launch level or in the troposphere. In this case we can just choose a very large amplitude and GROGRAT will cut down the amplitude in the first propagation step. Then the whole distribution depends only on propagation and saturation rules. The other extreme would be to use a very low

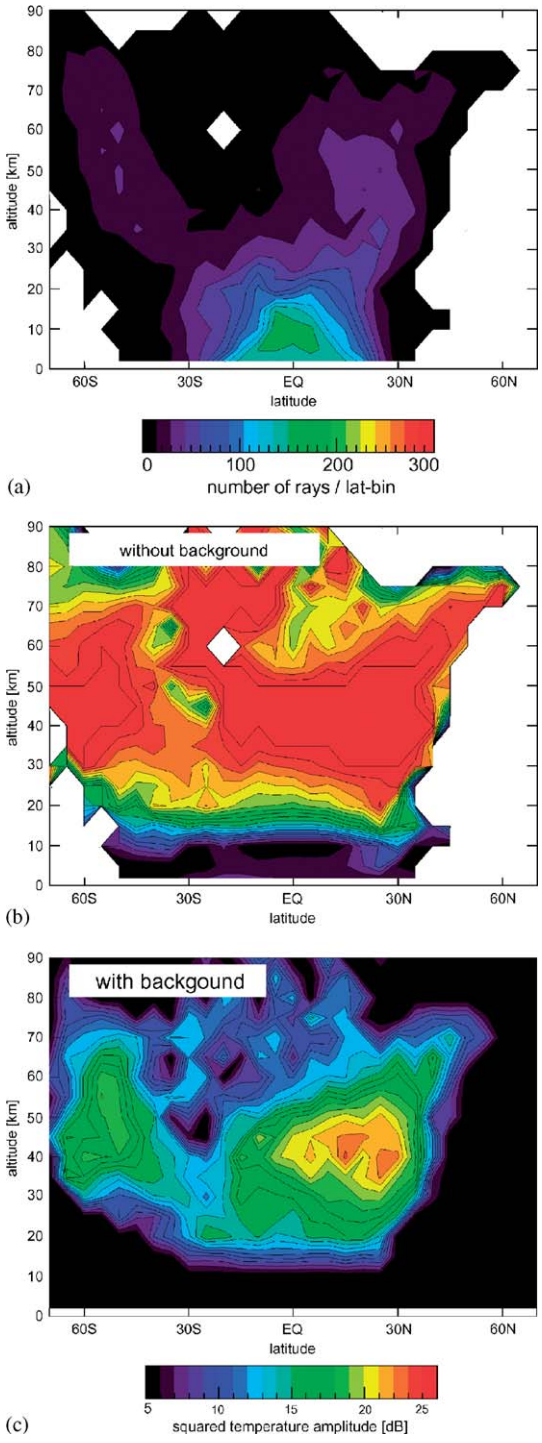

Fig. 4. Total number of rays in a latitude interval (panel a) and zonal mean-squared temperature amplitudes (panels b and c) for a $c = 30\,\mathrm{ms}^{-1}$, $\lambda_h = 3000\,\mathrm{km}$ spectral component experiment (SCE). Panels a and b show the result of the propagated rays only, panel c includes also a background. For details see text.

launch amplitude so that even at the highest altitudes amplitude growth is insufficient to reach saturation. In this case the whole distribution is simply proportional to the launch amplitude. For many spectral components a realistic representation is between these two extremal cases. The two extremal cases can be covered in one run to save computation time. In parallel to the saturated amplitudes, GROGRAT further propagates the unsaturated amplitudes, i.e. propagates an amplitude as if no saturation would exist. These unsaturated amplitudes can be considered when we are just interested in the shape of the global distribution caused by non-saturated rays.

In Fig. 5 we compare global maps of saturated and unsaturated temperature squared amplitudes for $c = 3$ and $10\,\mathrm{ms}^{-1}$ at 25 km altitude and $c = 30\,\mathrm{ms}^{-1}$ at 60 km altitude. The first two runs were launched with a very high amplitude and saturated directly in the first propagation step, the third SCE was launched with $1.0\,\mathrm{ms}^{-1}$ wind velocity amplitude and saturates at ~50 km altitude. At both altitudes only the saturated amplitudes map the planetary wave structure of the background winds into the GW distribution as we have observed in the CRISTA data. At 60 km we also compare $\lambda_h = 200$ km with $\lambda_h = 500$ km runs. The 500 km waves can propagate a bit further from the launch position and they hence result in somewhat smoother patterns but there is no difference in the major structures. This is mainly due to the fact that in the maps the upstream propagating waves dominate. These steepen up and reach the high altitudes very fast (Gerrard et al., 2004) in contrast to downstream propagating waves which sometimes can propagate nearly 360° longitude before reaching the upper mesosphere.

4.4. A survey of different phase speeds

We now make a systematic survey of single SCEs by showing zonal mean cross sections of temperature-squared amplitudes for various phase speeds and launch amplitudes. Since there is not much difference in the temperature variances of $\lambda_h = 200$ and 500 km runs, only results from the $\lambda_h = 200$ km runs are shown in Fig. 6. All results are filtered for instrument visibility by applying a $\lambda_z = [5, 25\,\mathrm{km}]$ vertical wavelength filter and a $\lambda_h > 100$ km cut-off. (Note that GROGRAT also alters the horizontal wavelength according to the ray-trace equations, Marks and Eckermann, 1995.) A representative launch distribution consists of several mesoscale horizontal wavelength components to be selected from Fig. 6 and needs to be completed by some very long wavelength components to match the equatorial maximum observed in climatologies. The launch amplitudes of the respective mesoscale runs are given in Table 1. As discussed above, the amplitudes of the saturated SCEs are very large, and the precise values are irrelevant.

The comparison of CRISTA measurements and Warner and McIntyre spectral modeling (cf. Section 3.4) confirms the original choice of tunable parameters. These are (Ern et al., 2004) a peak vertical wavelength of $\lambda_z^* = 2$ km at the launch level, and an approximately linear increase of momentum flux at low wavenumbers (i.e. inversely proportional to the wavelength). We can use these findings to guide the choice of launch amplitudes for GROGRAT. Using a tropospheric buoyancy period of roughly 10 min and zero background wind, Eq. (1) shows that $\lambda_z^* = 2$ km corresponds to a phase speed slightly larger than $c = 3\,\mathrm{ms}^{-1}$. The $c = 3\,\mathrm{ms}^{-1}$ SCE should therefore be launched saturated and, following this guidance, all higher phase speed SCEs should be non-saturated and launched with smaller amplitudes. However, comparing the values at 60°S in Fig. 6 with the measurements (Fig. 2), the $c = 3\,\mathrm{ms}^{-1}$ component is too strongly governed by the wind, i.e. the increase from 20 to 50 km altitude is too steep compared to the measurements. The saturated temperature amplitudes at $c = 10\,\mathrm{ms}^{-1}$ shown in Fig. 6c are maximum around 30 km and the increase between 20 and 30 km is weak. Not too much weight should be given to the absolute amplitude agreement, since there are two unknown variables, the launch amplitude as well as the intermittency. Since already the GW-squared amplitudes of the $c = 3\,\mathrm{ms}^{-1}$ component are larger than the measured values, intermittency will be required for compensation. To optimize for the shape at high southern latitudes and low altitudes, a low intermittency $c = 10\,\mathrm{ms}^{-1}$ component is used in the composite experiment (CPE) (Section 4.6).

All shown SCEs with exception of the $c = 50\,\mathrm{ms}^{-1}$ run are saturated in the entire mesosphere, i.e. at altitudes above 50 km. They all exhibit the northward shift of the GW maximum at the top of the stratospheric wind jet at ~60°S. This means we can investigate the phenomenon in the leading SCE. Since the saturation amplitude $\hat{T}_{\mathrm{sat}}$ is

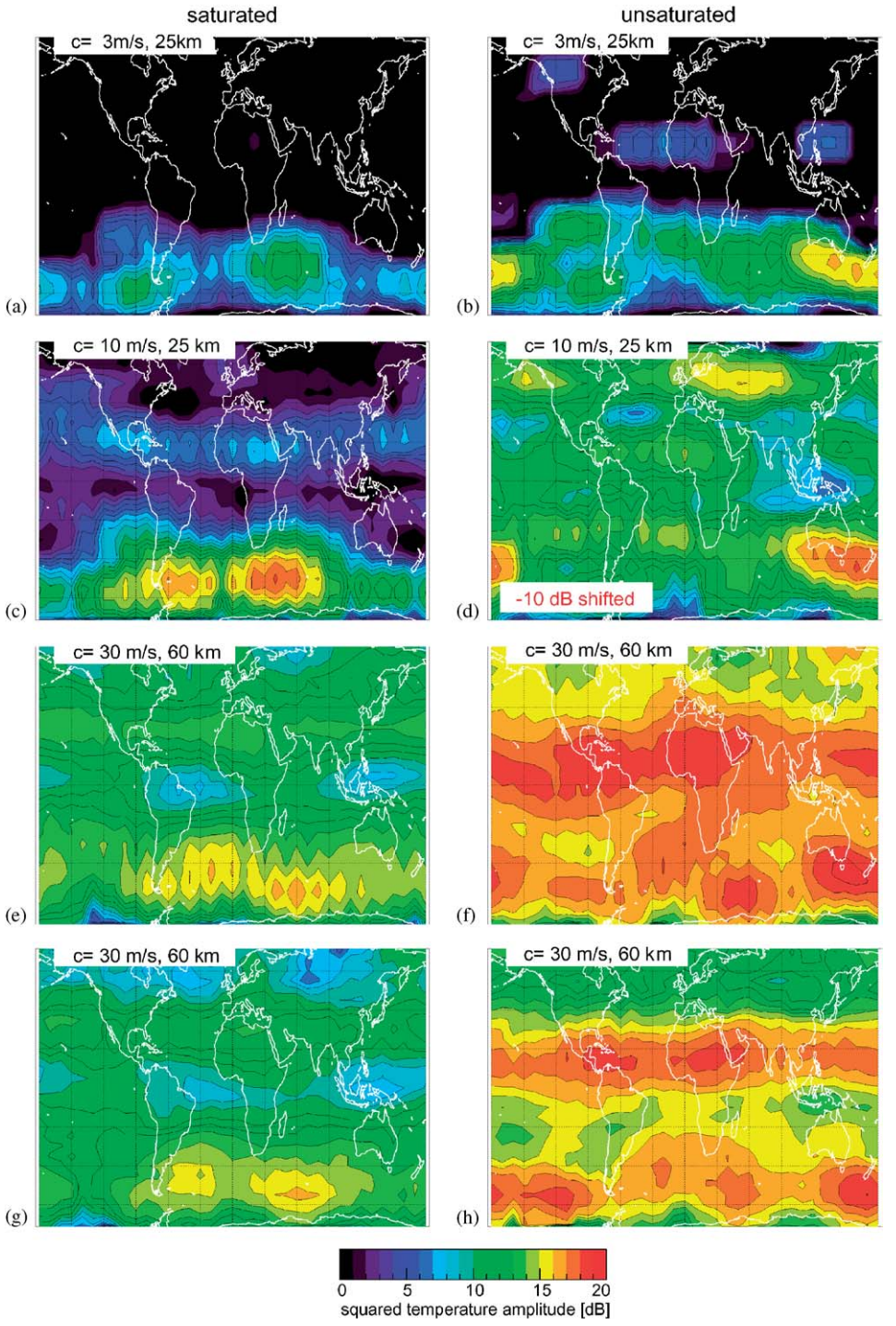

Fig. 5. Comparison of global distributions consisting of saturated (left) and unsaturated (right) GWs for 25 km (panels a–d) and 60 km (panels e–h) altitude. The third and fourth rows differ in the horizontal wavelength, which is $\lambda_h = 200$ and 500 km, respectively, at the launch level. For the unsaturated case only the shape of the distribution is meaningful. For saturated waves the amplitudes are limited by the saturation process and hence do not depend on the launch value. The color scale has been shifted by −10 dB for panel d.

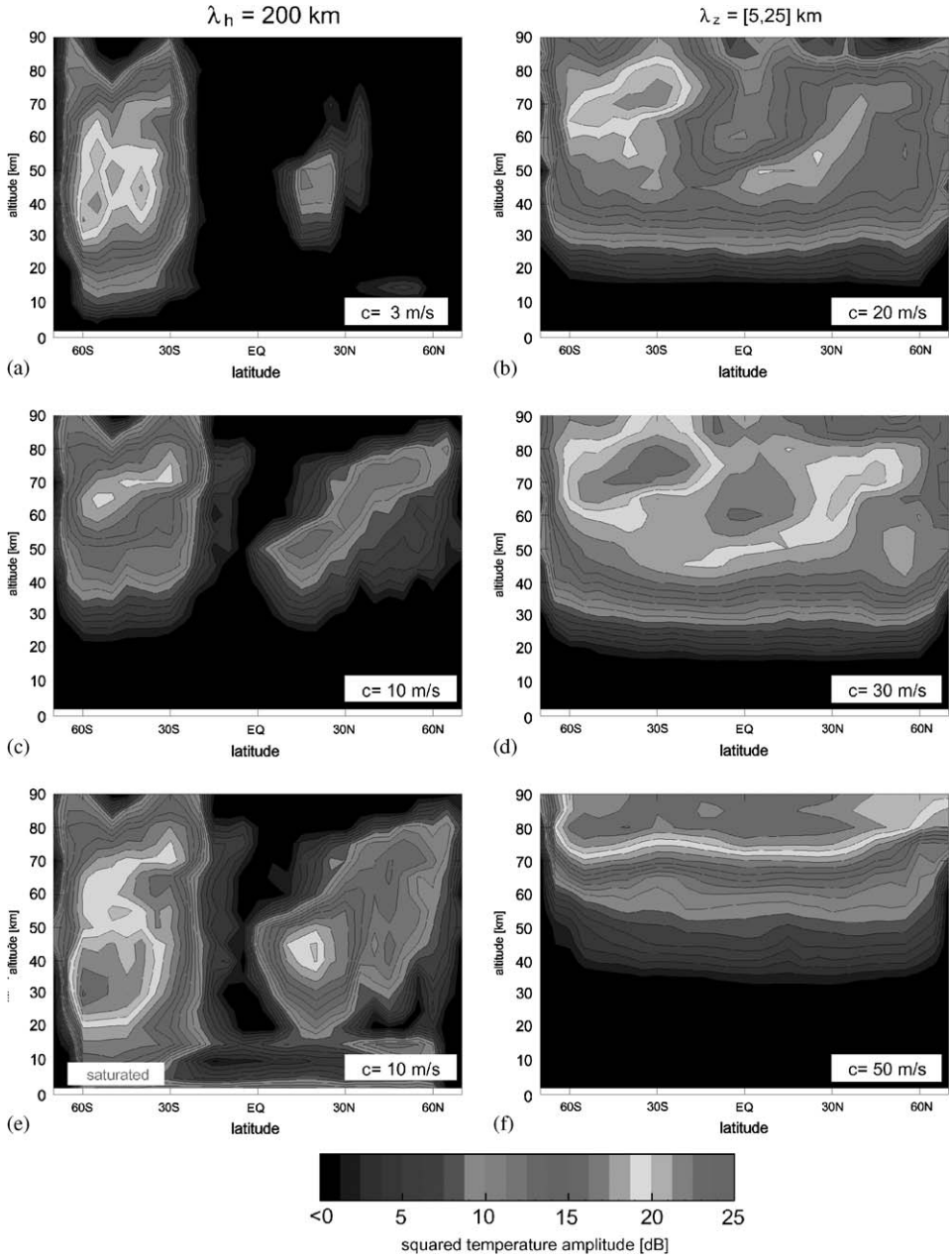

Fig. 6. Zonal mean GW-squared amplitudes from GROGRAT single component experiments of different phase speeds. The values are visibility filtered. For details see text.

proportional to the vertical wavelength (Eckermann and Preusse, 1999)

$$\hat{T}_{\mathrm{sat}} = \frac{\bar{T}}{g} N^2 \frac{\lambda_z}{2\pi} \tag{3}$$

the leading component at the top of the vortex is the $c = 30\,\mathrm{ms}^{-1}$ SCE.

4.5. Saturation versus visibility at the top of the jet

Fig. 7 shows the $c = 30\,\mathrm{ms}^{-1}$, $\lambda_\mathrm{h} = 200\,\mathrm{km}$ SCE. Compared are results from saturated and unsaturated amplitudes as well as visibility filtered and unfiltered distributions. Visibility filtering introduces only a slight low bias, whereas saturation

completely alters the distribution. All important structures seen in the observations are found only in the saturated amplitudes. This is evidence that wave breaking is the dominating process in the activity decrease at the top of the stratospheric jet. The same experiment with $\lambda_h = 500$ km (not shown) results in very similar distributions, an indication that slant wave propagation plays only a minor role in explaining this feature, too.

Table 1
Phase speeds and amplitudes for the individual SCEs shown in Fig. 6

Panel	Phase speed (ms^{-1})	Launch ampl. (ms^{-1})
(a)	3	6.0
(b)	10	1.0
(c)	10	20.0
(d)	20	1.4
(e)	30	1.0
(f)	50	0.2

4.6. Concocting a composed GROGRAT launch distribution

The composition of a comprehensive GW launch distribution for GROGRAT can be motivated by the results of this section as well as previous studies (cf. Section 3), but the result will only be straightforward to a certain degree and the solution cannot be proven to be unique. We know that we have to include a $c = 3\,ms^{-1}$ saturated SCE and likely an $c = 10\,ms^{-1}$ saturated SCE of mesoscale waves (λ_h of the order of a few 100 km). We know from CRISTA spectral investigations (Preusse et al., 2001b) that high phase speeds, e.g. $c = 50\,ms^{-1}$, are also part of the spectrum and that the amplitudes should decrease towards higher phase speeds. We see that the $c = 50\,ms^{-1}$ component is required to maintain some variance at the highest

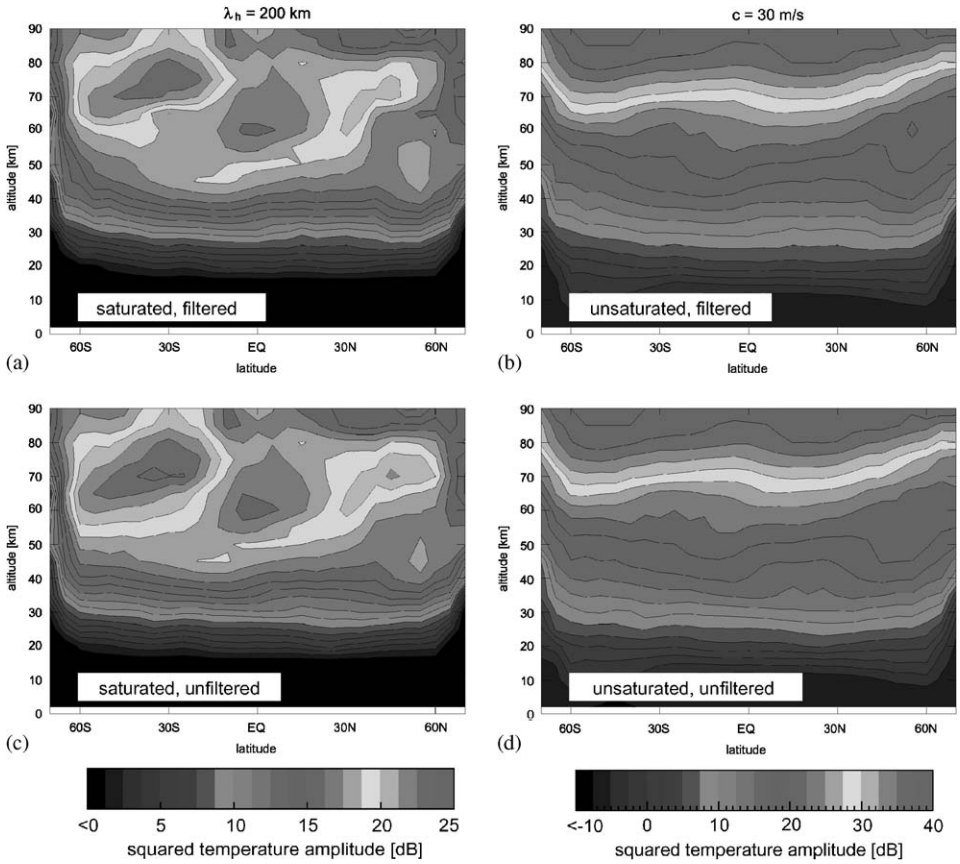

Fig. 7. SCE with $c = 30\,ms^{-1}$ and $\lambda_h = 200$ km. Comparison of results from saturated and unsaturated amplitudes, visibility filtered and unfiltered. Visibility filtering induces only a minor offset whereas saturation shapes the global distributions.

altitudes above 75 km, which would otherwise be underestimated. Also, the higher phase speeds are less likely to occur, i.e. they have a low intermittency. Including in a CPE a saturated (at launch level) $c = 30\,\mathrm{ms}^{-1}$ component would result in a large overestimation of the observed amplitudes. We also can follow the suggestion from the spectral models that the decrease at longer vertical wavelengths, i.e. higher phase speeds, is approximately proportional to the vertical wavenumber. All these arguments together give us an idea of the mesoscale components. In addition, we have some very long horizontal wavelength components.

From this guidance we construct two composites which differ in the horizontal wavelength of the mesoscale components. The details are specified in Table 2. The resulting distributions are shown in Fig. 8. As indicated in Table 2, we must maintain a large background component to represent intermittency. This is in agreement with the observations (cf. Preusse et al., 2003a). A substantial reduction of the background would result in unreasonably high variances and momentum flux values. The background values for the squared amplitudes (Fig. 8a–d) are $0.5^2\,\mathrm{K}^2$, the background momentum flux values are 10^{-9} Pa (Fig. 8g and h). Since there is no information at all about the wavelength distribution of a background, we present in Fig. 8e and f the wavelength distribution generated by the actual GROGRAT rays only.

The squared temperature amplitudes (Fig. 8a–d) for the two CPEs are nearly equal. They match the measured distributions well, with two exceptions: at middle and high northern latitudes there is only a slight decrease. (Please note that due to the wind field boundaries at 70° latitude and the launch grid of an SCE the highest latitudes have only a strongly decreased number of ray events and that therefore at all latitudes higher than 60° the GROGRAT mean values are not fully reliable and underestimated.) A flat distribution towards high latitudes is in disagreement with the satellite measurements in Fig. 2 which show very narrow contour spacing, i.e. a huge gradient of the GW activity towards the pole. We will come back to this point when we have further evidence from the Warner and McIntyre modeling in Section 5. The second exception is the underestimate of wave activity in the northern subtropics above 50 km altitude. It is evident from Fig. 6 that only a fast phase speed (cf. panel f, $c = 50\,\mathrm{ms}^{-1}$) can fill in the missing wave activity, since all other components are saturated and decrease above 50 km. (There is already a slight overestimate of wave activity in the tropics/NH subtropics at ~40 km, which, however, cannot propagate upward.)

The horizontal wavelength distribution is a further test of how realistic the composite modeling experiment is. Though we have already included a $\lambda_h = 6000$ km launch wavelength SCE with enhanced intermittency, the average horizontal wavelength (Fig. 8f) is still smaller than in the experimental data (Fig. 3). The distribution agrees with the data in the smooth decrease of wave activity at higher latitudes, however, the observed dip of horizontal wavelength in the northern subtropics is not reproduced.

The momentum flux values of the longer horizontal wavelength $\lambda_h = 500$ km CPE (Fig. 8h) are in good agreement with the values published by Preusse et al. (2003b) and Ern et al. (2004). Approximate values in the lower stratosphere are:

Table 2
Components of a representative GW launch spectrum composed from several single SCEs

Horizontal wavel. (km)	Phase speed (ms^{-1})	Amplitude (ms^{-1})	Intermittency factor	Remark
–	–	0.5	5.0	Background
200/500	3	6.0	1.0	Saturated
200/500	10	20.0	0.4	Saturated
200/500	30	1.0	1.0	
200/500	50	0.2	0.5	
2000	30	1.0	1.0	
3000	30	6.0	1.0	Large area
6000	30	30.0	2.0	Saturated

Mesoscale horizontal wavelength can be either $\lambda_h = 200$ or 500 km.

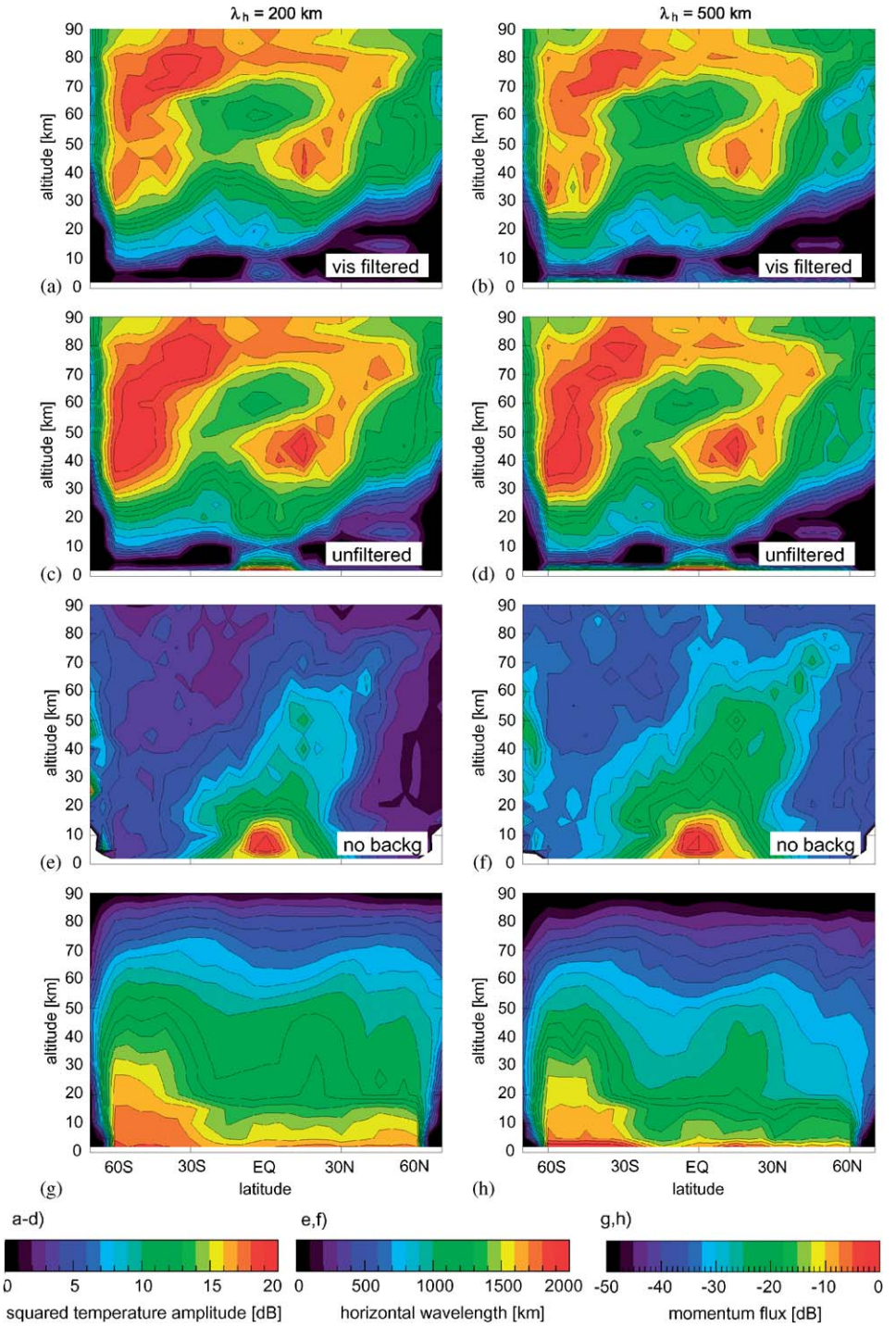

Fig. 8. Squared GW temperature amplitudes (a–d), average horizontal wavelengths (e,f) and momentum flux (g,h) for two composed GW launch distributions. The two composed experiments differ in the horizontal wavelength of the mesoscale components. The reference level for converting the momentum flux into dB is 1 Pa.

in the polar vortex ~ -12 dB, in the tropics (20°S–10°S) -26 dB, in the NH subtropics -23 dB and at 60°N, the highest latitude with reliable values, -30 dB, corresponding to approximately 63, 2.5, 5 and 1.0 mPa, respectively. Note that the reference level for the momentum flux is 1 Pa.

This is roughly a factor of 2 higher than the CRISTA values of 20, 1.5, 3 and 2 mPa (cf. Fig. 7 of Preusse et al., 2003b and Fig. 3 of Ern et al., 2004).

The overestimation likely indicates that the $c = 10\,\mathrm{ms}^{-1}$ saturated component is too strong. The momentum flux of a saturated SCE is very sensitive to the vertical wavelength and hence the phase speed of the fastest saturated component. Both the momentum flux of a given GW and the saturation amplitude are proportional to the vertical wavelength. Calculating the momentum flux F_{ph} of a saturated wave we find

$$F_{\mathrm{ph}} \sim \frac{\lambda_z}{\lambda_{\mathrm{h}}} \hat{T}^2_{\mathrm{sat}} \sim \lambda_z^3. \tag{4}$$

The momentum flux of a saturated SCE is therefore proportional to the third power of the vertical wavelength of the waves. Thus, one could likely find a better agreement by either reducing the intermittency weight on the $c = 10\,\mathrm{ms}^{-1}$ SCE or replacing the saturated $c = 10\,\mathrm{ms}^{-1}$ SCE by a saturated SCE of a phase speed between 3 and $10\,\mathrm{ms}^{-1}$.

The values in Fig. 8g stemming from the $\lambda_{\mathrm{h}} = 200\,\mathrm{km}$ CPE are about 4 dB higher than those of the $\lambda_{\mathrm{h}} = 500\,\mathrm{km}$ CPE (Fig. 8h), because momentum flux is inversely proportional to the horizontal wavelength. This means the horizontal wavelength is an additional tuning parameter to fit the momentum flux. It appears therefore unwise to do more fine tuning before further experimental facts provide a more detailed guidance.

Indications for more fundamental problems are found in the NH. The missing dip in the horizontal wavelength and the need for more high phase speed waves at mesospheric altitudes indicate that the NH subtropical band of convectively generated GWs needs to be explicitly included in the launch distribution. On the other hand, we have too much forcing at the high summer latitudes. Both are points which cannot be solved by a small tuning of the homogeneous source distribution but require the introduction of source non-homogeneity.

5. Warner and McIntyre modeling

The Warner and McIntyre (WM) spectral model approach is much more straightforward than the GROGRAT approach. First, because the model provides a clear spectral concept and second, because we can rely on previous studies which largely confine the range of tunable parameters. The experiment discussed here uses a launch level of 2 km, a critical wavelength of $\lambda_z^* = 2\,\mathrm{km}$ and a slope of the non-saturated part of +1. The resulting momentum flux values, with and without visibility filtering, as well as the resulting wind accelerations are shown in Fig. 9. Plots are generated for two different ways of displaying the momentum flux. The upper row gives the momentum flux in Pa or $\mathrm{kg\,m^{-1}\,s^{-2}}$, the lower row the mass-free momentum flux (momentum flux divided by density) in $\mathrm{m^2\,s^{-2}}$. The structures of the first row are dominated by the mass decrease with altitude, the structures of the second row are closer to the behavior of the squared temperature amplitudes. The momentum flux values (in Pa) have the same scale as the GROGRAT momentum flux values given in Fig. 8. It is evident that visibility filtering strongly influences the structure of the observed stratospheric values but introduces only a small offset in the mesosphere. In particular, the depletion of wave momentum in the NH substantially increases the correlation between measurements and modeling (Ern et al., 2005).

The WM modeling results reproduce the observed northward shift at the top of the stratospheric wind jet. Though the absolute values are different, the shape is very similar in visibility filtered and unfiltered results. This corroborates our findings from GROGRAT that primarily wave breaking is responsible for the amplitude decrease at the top of the jet. The WM model then enables us to calculate also wind accelerations. The wind acceleration shows a pronounced maximum at the top of the jet, just at the position of maximum wave-activity decrease.

Momentum flux values shown in Figs. 8 and 9 can be compared to estimates from airglow imaging measurements (Espy et al., 2006). It should be noted that the airglow imager is sensitive to short horizontal wavelengths $< 150\,\mathrm{km}$. At 90 km altitude the momentum flux values shown in Fig. 8 correspond to 2 and $5\,\mathrm{m^2\,s^{-2}}$ for the $\lambda_x = 500$ and 200 km CPE, respectively. The unfiltered WM modeling results are $\sim 3\,\mathrm{m^2\,s^{-2}}$. This is of the same size as the data taken at Halley (76°S, 27°W), but is an order of magnitude smaller than the values from Rothera (67°S, 68°W) on the Antarctic Peninsula. This indicates that additional, localized sources are required to fully describe the global distributions.

Considering the NH both models agree in that they grossly overestimate the summer high latitude activity. The WM modeling indicates nearly

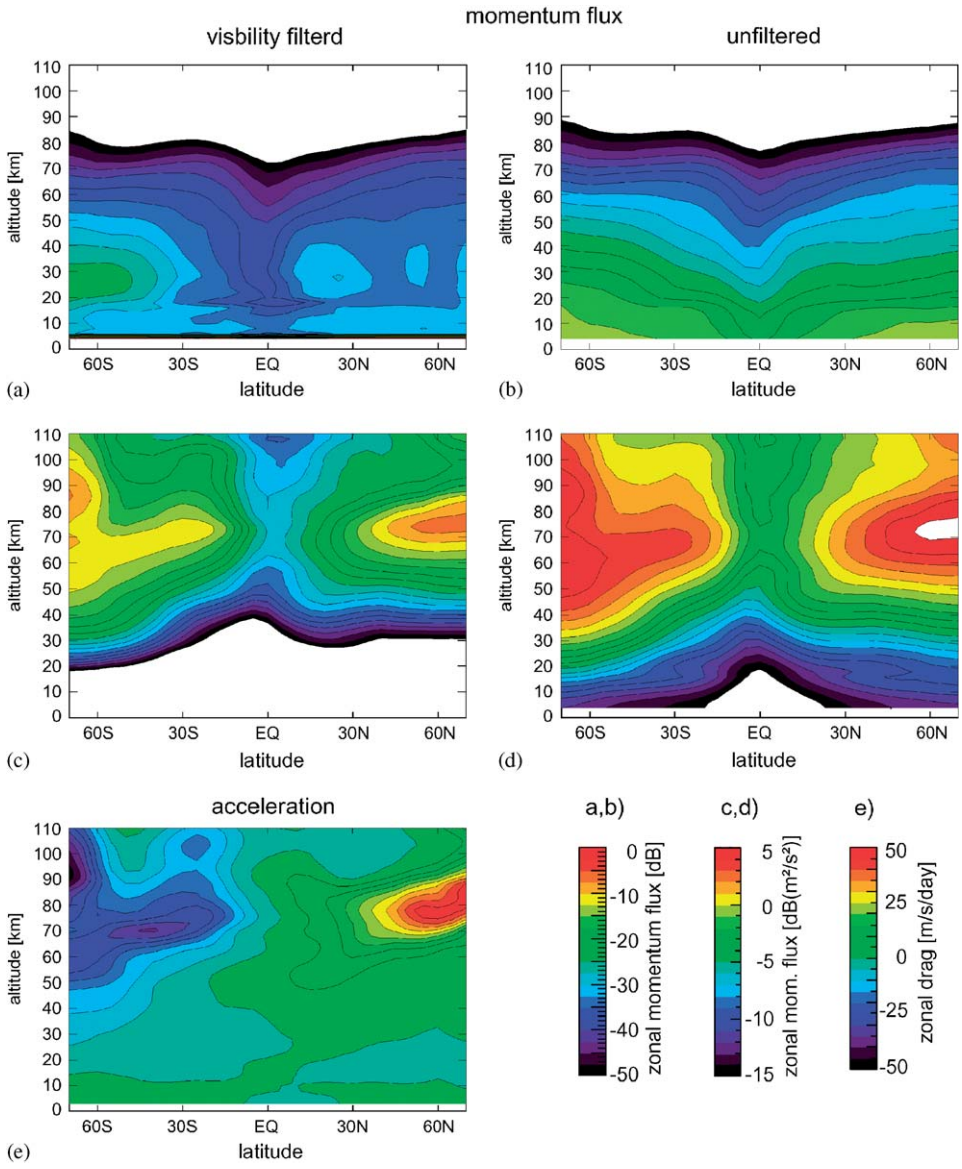

Fig. 9. Absolute values of momentum flux and zonal wind accelerations as modeled by the Warner and McIntyre spectral parameterization scheme. Momentum flux is shown with (left) and without (right) visibility filter applied. When given in Pa (first row) the altitude structure is dominated by the density decrease, while when given in $m^2 s^{-2}$ the distribution is closer to that of the squared temperature amplitudes.

hemispheric symmetry, i.e. summer (NH) and winter (SH) values are very similar. This is in contradiction to the CRISTA and SABER measurements, where we observe a steep decrease at high latitudes of the summer hemisphere. It is also in contradiction to mesospheric lidar measurements from Kühlungsborn (~54 N) and ALOMAR (~70 N) (Lübken personal communication; Rauthe et al., 2004, 2006). At the mid-latitude station only a moderate summer to winter difference is observed (a factor 2–3), at higher latitudes the summer to winter difference is about a factor of 5 or larger. The large summer to winter difference at high latitudes is also observed in mesospheric rocket climatologies (Lübken and von Zahn, 1991) (please note that the RMS values in Lübken and von Zahn (1991) also include a height-independent offset, which is likely not due to GWs). The corroboration by in situ and lidar measurements is particularly interesting, since there is no limit to the horizontal wavelength by

these techniques, which, however, is implied by the visibility filter of the satellite data.

Since we observe the excess in modeled high latitude GW activity in the summer hemisphere in both studies, performed with two conceptually different models and since we start at a low launch level, this is evidence that wind filtering cannot serve in sufficiently reducing the wave activity in the high altitude, high latitude summer hemisphere. Instead, a non-homogeneous GW source is required, which is substantially smaller at high summer latitudes and which is larger in the northern subtropics above convection.

6. Summary and conclusion

We present and compare global distributions of gravity wave (GW) activity measured by two different infrared emission limb sounders, the CRISTA and the SABER instrument, in August 1997 and August 2003, respectively. Though some differences exist, the data agree in their salient features: very strong activity at the edge of the stratospheric southern polar winter vortex, a quiet Northern summer hemisphere, a tropical maximum, which is particularly pronounced at lower altitudes, pronounced GW maxima above convection regions in the northern (summer) subtropics, and indications of mountain waves above the Southern-tip of South America and the Antarctic Peninsula. One major difference between the two data sets is the presence of strong planetary waves during the CRISTA period which are imaged in the GW distribution. Of particular interest in this paper is the decrease of GW variance at the top of the stratospheric winter polar vortex and the shift of GW activity towards a subtropical mesospheric jet, which is common to both measurements.

In order to understand this and other salient features we have employed GW modeling relying on two conceptually different models, the Warner and McIntyre spectral parameterization scheme, which is designed for operating within GCMs, and the GROGRAT GW ray tracer, which is designed for case studies like the present one. Both models were run in a composite wind field of meteorological reanalysis, CRISTA geostrophic winds, and CIRA climatological data. This composite was created to provide wind fields as realistic as possible from the ground to the lower thermosphere.

For both models we launched isotropic GW distributions at 2 km altitude. The launch distribution of GROGRAT is homogeneous, while the launch distribution of the WM scheme has a simple latitude dependence, which results from the pre-integration of the horizontal wavelength spectrum. The optimum launch parameters for the WM scheme were adopted from comparisons to stratospheric GW momentum flux estimates (Ern et al., 2004, 2005, 2006). The GROGRAT model enables us to study the influence of different spectral components separately. This conceptional advantage becomes a difficulty when generating a representative spectrum, since the solution is not unique.

Both models are successful in capturing most of the salient features observed in the data. Exceptions are the regions of distinctive sources, i.e. the mountain waves downstream of the Andes and the NH subtropical convection. These were expected. Unexpected, however, is a gross overestimate of wave activity at high northern (summer) latitudes. This low activity at high latitudes is corroborated by LIDAR and in situ measurements, i.e. completely different measurement techniques. Both models, which are completely different in their conception of wave propagation, produce this overestimate. This is a hint that a uniform source distribution might be generally unable to reproduce even major structures of the real GW distribution and the resulting wind accelerations. The models are very successful in explaining the decrease of GW activity at the top of the southern polar vortex and the shift of activity towards the subtropics. The phenomenon is due to favorable propagation conditions in the strong winds of the jets and due to enhanced wave breaking on top of these jets, due to Doppler shift to lower vertical wavelengths and resulting smaller instability amplitude limits. Visibility filtering and slant wave propagation are minor effects in explaining this feature. The phenomenon can be reproduced by waves in a wide range of phase speeds and horizontal wavelengths.

Some important puzzles remain unsolved. The constraints imposed by the data are insufficient to find a unique solution in terms of the horizontal wavelength distribution and the balance between amplitude and intermittency; with large consequences for the carried momentum flux. Also, we can attribute a large part of the observed GW global distribution to a homogeneous source distribution. The nature of this source remains as obscure as before. However, the failure to describe the northern high latitudes shows that a better understanding

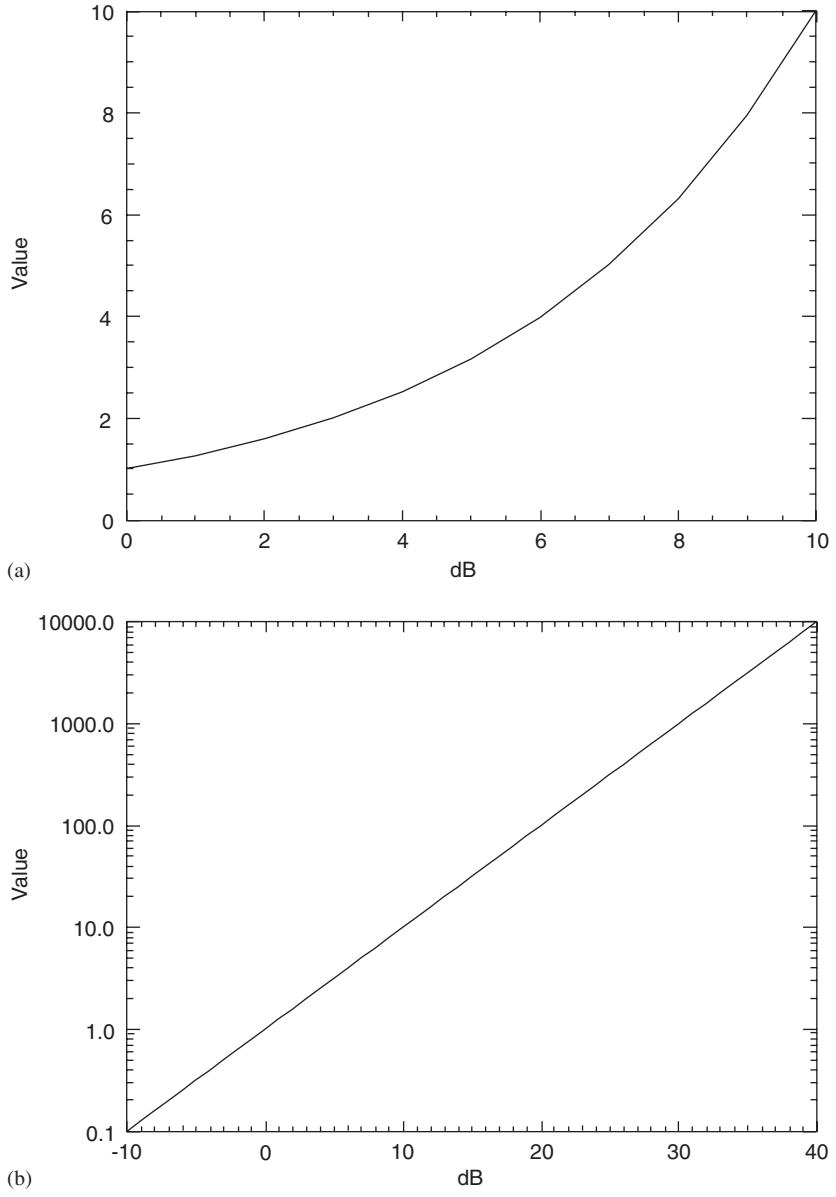

Fig. 10. Conversion between values of parameters and corresponding dB values.

of the sources is imperative. Global measurements of high spatial resolution 3D temperature fields could enable us to better constrain the horizontal wavelengths and to understand the nature of the sources in case studies. First steps could be made by a reprogramming of the SABER measurement modes in order to achieve a substantially shorter along- track distance between the profiles, which would provide at least high resolution 2D pictures. Current technique provides the potential to obtain high 3D spatial resolution by limb imaging (Riese et al., 2005; Friedl-Vallon et al., 2006).

Acknowledgments

This work is partially funded through DFG project GW-CODE (ER 474/1-1), DFG priority program CAWSES SPP 1176; the Air Force Office of Scientific Research (Kent Miller), and the NASA SABER Program Office at NASA Langley

Research Center. We thank Dr Jens Oberheide for providing the CRISTA geostrophic wind fields.

Appendix

Many of the values in this paper are given in dB, which is defined by

$$dB = 10 * \log_{10}(\text{value}). \quad (5)$$

For a quick conversion, however, a graph might be preferable, which is provided in Fig. 10.

References

Alexander, M.J., 1998. Interpretations of observed climatological patterns in stratospheric gravity wave variance. Journal of Geophysical Research 103, 8627–8640.

Alexander, M.J., Beres, J.H., Pfister, L., 2000. Tropical stratospheric gravity wave activity and relationships to clouds. Journal of Geophysical Research 105, 22299–22309.

Alexander, M.J., Tsuda, T., Vincent, R.A., 2002. On the latitudinal variations observed in gravity waves with short vertical wavelengths. Journal of Atmospheric Science 59, 1394–1404.

Allen, S.J., Vincent, R.A., 1995. Gravity wave activity in the lower atmosphere: seasonal and latitudinal variations. Journal of Geophysical Research 100, 1327–1350.

Bacmeister, J.T., Eckermann, S.D., Newman, P.A., Lait, L., Chan, K.R., Loewenstein, M., Porffitt, M.H., Gary, B.L., 1996. Stratospheric horizontal wavenumber spectra of winds, potential temperature, and atmospheric tracers observed by high-altitude aircraft. Journal of Geophysical Research 101, 9,441–9,470.

Beres, J.H., Garcia, R.R., Boville, B.A., Sassi, F., 2005. Implementation of a gravity wave source spectrum parameterization dependent on the properties of convection in the Whole Atmosphere Community Climate Model (WACCM). Journal of Geophysical Research 110, D10108.

Chandra, S., Fleming, E.L., Schoeberl, M.R., Barnett, J.J., 1990. Monthly mean global climatology of temperature, wind, geopotential height and pressure for 0−120 km. Advances in Space Research 10, 3–12.

Chun, H.-Y., Song, I.-S., Baik, J.-J., Kim, Y.-J., 2004. Impact of a convectively forced gravity wave drag parameterization in NCAR CCM3. Journal of Climate 17, 3530–3547.

Coy, L., Swinbank, R., 1997. Characteristics of stratospheric winds and temperatures produced by data assimilation. Journal of Geophysical Research 102, 25,763–25,781.

Dewan, E.M., 1997. Saturated-cascade similitude theory of gravity-wave spectra. Journal of Geophysical Research 102, 29,799–29,817.

Eckermann, S.D., Marks, C.J., 1997. GROGRAT: a new model of the global propagation and dissipation of atmospheric gravity waves. Advances in Space Research 20, 1253–1256.

Eckermann, S.D., Preusse, P., 1999. Global measurements of stratospheric mountain waves from space. Science 286, 1534–1537.

Eidmann, G., Offermann, D., Preusse, P., 2001. Fluctuation power spectra in the mid stratosphere at increased horizontal resolution. Advances in Space Research 27, 1647–1652.

Ern, M., Preusse, P., Alexander, M.J., Warner, C.D., 2004. Absolute values of gravity wave momentum flux derived from satellite data. Journal of Geophysical Research 109, D20103.

Ern, M., Preusse, P., Warner, C.D., 2005. A comparison between CRISTA satellite data and Warner and McIntyre gravity wave parameterization scheme: horizontal and vertical wavelength filtering of gravity wave momentum flux. Advances in Space Research 35, 2017–2023.

Ern, M., Preusse, P., Warner, C.D., 2006. Some experimental constraints for parameters used in the Warner and McIntyre gravity wave parameterization scheme. Atmospheric Chemistry and Physics Discussions 6, 4755–4794.

Espy, P.J., Hibbins, R.E., Swenson, G.R., Tang, J., Taylor, M.J., Riggin, D.M., Fritts, D.C., 2006. Regional variations of mesospheric gravity-wave momentum flux over Antarctica. Annales Geophysicae 24, 81–88.

Fetzer, E.J., Gille, J.C., 1994. Gravity wave variances in LIMS temperatures, I, Variability and comparison with background winds. Journal of Atmospheric Science 51, 2461–2483.

Friedl-Vallon, F., Riese, M., Maucher, G., Lengel, A., Hase, F., Preusse, P., Spang, R., 2006. Instrument concept and preliminary performance analysis of GLORIA. Advances in Space Research 37, 2287–2291.

Fritts, D.C., Alexander, M.J., 2003. Gravity wave dynamics and effects in the middle atmosphere. Reviews in Geophysics 41 art. no. 1003.

Gerrard, A.J., Kane, T.J., Eckermann, S.D., Thayer, J.P., 2004. Gravity waves and mesospheric clouds in the summer middle atmosphere: a comparison of lidar measurements and ray modeling of gravity waves over Sondrestrom, Greenland. Journal of Geophysical Research 109, D10103.

Grossmann, K.U., Offermann, D., Gusev, O., Oberheide, J., Riese, M., Spang, R., 2002. ISTA-2 Mission. Journal of Geophysical Research 107, 8173.

Hertzog, A., Vial, F., Mechoso, C.R., Badesavant, C., Cocquerez, P., 2002. Quasi-Lagrangian measurements in the lower stratosphere reveal an energy peak associated with near-inertial waves. Geophysics Research Letters 29, 1229.

Jiang, J.H., Eckermann, S.D., Wu, D.L., Ma, J., 2004a. A search for mountain waves in MLS stratospheric limb radiances from the winter Northern Hemisphere: data analysis and global mountain wave modeling. Journal of Geophysical Research 109, D03107.

Jiang, J.H., Wang, B., Goya, K., Hocke, K., Eckermann, S.D., Ma, J., Wu, D.L., Read, W.J., 2004b. Geographical distribution and interseasonal variability of tropical deep convection: UARS MLS observations and analyses. Journal of Geophysical Research 109, D03111.

Lange, M., Jacobi, Ch., 2003. Analysis of gravity waves from radio occultation measurements. In: Reigber, Ch., Lühr, H., Schwintzer, P. (Eds.), First CHAMP Mission Results for Gravity, Magnetic and Atmospheric Studies. Springer, Berlin, pp. 479–484.

Lübken, F.-J., von Zahn, U., 1991. Thermal structure of the mesopause region at polar latitudes. Journal of Geophysical Research 96, 20,841–20,857.

Marks, C.J., Eckermann, S.D., 1995. A three-dimensional nonhydrostatic ray-tracing model for gravity waves: formulation and preliminary results for the middle atmosphere. Journal of Atmospheric Science 52, 1959–1984.

McFarlane, N.A., 1987. The effect of orographically excited gravity wave drag on the general circulation of the lower stratosphere and troposphere. Journal of Atmospheric Science 44, 1775–1800.

McLandress, C., Alexander, M.J., Wu, D.L., 2000. Microwave Limb Sounder observations of gravity waves in the stratosphere: a climatology and interpretation. Journal of Geophysical Research 105, 11,947–11,967.

Mertens, C.J., Schmidlin, F.J., Goldberg, R.A., Remsberg, E.E., Pesnell, W.D., Russel III, J.M., Mlynczak, M.G., Lopez-Puertas, M., Wintersteiner, P.P., Picard, R.H., Winick, J.R., Gordley, L.L., 2004. SABER observations of mesospheric temperatures and comparisons with falling sphere measurements taken during the 2002 summer MaCWAVE campaign. Geophysics Research Letters 31, L03105.

Mlynczak, M.G., 1997. Energetics of the mesosphere and lower thermosphere and the SABER experiment. Advances in Space Research 20, 1177–1183.

Oberheide, J., Hagan, M.E., Ward, W.E., Riese, M., Offermann, D., 2000. Modeling the diurnal tide for CRISTA 1 time period. Journal of Geophysical Research 105, 24,917–24,929.

Oberheide, J., Lehmacher, G.A., Offermann, D., Grossmann, K.U., Manson, A.H., Meek, C.E., Schmidlin, F.J., Singer, W., Hoffmann, P., Vincent, R.A., 2002. Geostrophic wind fields in the stratosphere and mesosphere from satellite data. Journal of Geophysical Research 107, 8175.

Offermann, D., Grossmann, K.U., Barthol, P., Knieling, P., Riese, M., Trant, R., 1999. The CRyogenic Infrared Spectrometers and Telescopes for the Atmosphere (CRISTA) experiment and middle atmosphere variability. Journal of Geophysical Research 104, 16,311–16,325.

Pfister, L., Scott, S., Loewenstein, M., Bowen, S., Legg, M., 1993. Mesoscale disturbances in the tropical stratosphere excited by convection: observations and effects on the stratospheric momentum budget. Journal of Atmospheric Science 50, 1058–1075.

Picard, R.H., O'Neil, R.R., Gardiner, H.A., Gibson, J., Winick, J.R., Gallery, W.O., Stair, A.T., Wintersteiner, P.P., Shegblom, E.R., Richards, E., 1998. Remote sensing of discrete stratospheric gravity-wave structure at 4.3 mm from the MSX satellite. Geophysics Research Letters 25, 2809–2812.

Preusse, P., Ern, M., 2005. Indication of convectively generated gravity waves observed by CLAES. Advances in Space Research 35, 1987–1991.

Preusse, P., Schaeler, B., Bacmeister, J., Offermann, D., 1999. Evidence for gravity waves in CRISTA temperatures. Advances in Space Research 24, 1601–1604.

Preusse, P., Eckermann, S.D., Offermann, D., 2000. Comparison of global distributions of zonal-mean gravity wave variance inferred from different satellite measurements. Geophysics Research Letters 27, 3877–3880.

Preusse, P., Eckermann, S.D., Oberheide, J., Hagan, M.E., Offermann, D., 2001a. Modulation of gravity waves by tides as seen in CRISTA temperatures. Advances in Space Research 27, 1773–1778.

Preusse, P., Eidmann, G., Eckermann, S.D., Schaeler, B., Spang, R., Offermann, D., 2001b. Indications of convectively generated gravity waves in CRISTA temperatures. Advances in Space Research 27, 1653–1658.

Preusse, P., Dörnbrack, A., Eckermann, S.D., Riese, M., Schaeler, B., Bacmeister, J., Broutman, D., Grossmann, K.U., 2002. Space based measurements of stratospheric mountain waves by CRISTA, 1. Sensitivity, analysis method and a case study. Journal of Geophysical Research 107, 8178.

Preusse, P., Eckermann, S.D., Ern, M., Schmidlin, F.J., Alexander, M.J., Offermann, D., 2003a. Infrared limb sounding measurements of middle atmosphere gravity waves by CRISTA. SPIE Proceedings 4882, 134–148.

Preusse, P., Ern, M., Chen, Z., Offermann, D., 2003b. CRISCA: investigation of gravity waves based on satellite measurements. AFO Newsletter 5, 3–6 December.

Preusse, P., Ern, M., Grossmann, K.U., Mergenthaler, J.L., 2004. Seasonal variations of gravity wave variance inferred from CLAES. SPIE Proceedings 5235, 288–297.

Rauthe, M., Gerding, M., Berger, U., 2004. Lidarmessungen der Temperatur zwischen 1 und 105 km über Kühlungsborn zur Analyse von Schwerewellen. Proceedings DACH 2004, CD, 081_RaGeBe.pdf.

Rauthe, M., Gerding, M., Höffner, J., Lübken, F.-J. 2006. Lidar temperature measurements of gravity waves over Kühlungsborn (54° N) from 1–105 km: a winter–summer comparison. Journal of Geophysical Research, in press.

Riese, M., Spang, R., Preusse, P., Ern, M., Jarisch, M., Offermann, D., Grossmann, K.U., 1999. Cryogenic Infrared Spectrometers and Telescopes for the Atmosphere (CRISTA) data processing and atmospheric temperature and trace gas retrieval. Journal of Geophysical Research 104, 16,349–16,367.

Riese, M., Manney, G.L., Oberheide, J., Tie, X., Spang, R., Kuell, V., 2002. Stratospheric transport by planetary wave mixing as observed during CRISTA-2. Journal of Geophysical Research 107, 8179.

Riese, M., Friedl-Vallon, F., Spang, R., Preusse, P., Schiller, C., Hoffmann, L., Konopka, P., Oelhaf, H., von Clarmann, T., Höpfner, M., 2005. GLObal limb Radiance Imager for the Atmosphere (GLORIA): scientific objectives. Advances in Space Research 36, 989–995.

Russell III, J.M., Mlynczak, M.G., Gordley, L.L., Tansock, J., Esplin, R., 1999. An overview of the SABER experiment and preliminary calibration results. Proceedings of SPIE 3756, 277–288.

Tsuda, T., Nishida, M., Rocken, C., Ware, R.H., 2000. A global morphology of gravity wave activity in the stratosphere revealed by the GPS occultation data (GPS/MET). Journal of Geophysical Research 105, 7257–7273.

Warner, C.D., McIntyre, M.E., 1999. Toward an ultra-simple spectral gravity wave parameterization for general circulation models. Earth Planets Space 51, 475–484.

Warner, C.D., McIntyre, M.E., 2001. An ultra-simple spectral parameterization for non-orographic gravity waves. Journal of Atmospheric Science 58, 1837–1857.

Wu, D.L., 2001. Horizontal wavenumber spectra of MLS radiance fluctuations. Journal of Atmosphere Solar Terrestrial Physics 63, 1465–1477.

Wu, D.L., Waters, J.W., 1996. Gravity-wave-scale temperature fluctuations seen by the UARS MLS. Geophysics Research Letters 23, 3289–3292.

Yee, J.H., Talaat, E.R., Christensen, A.B., Killeen, T.L., Russell, J.M., Woods, T.N., 2003. TIMED instruments. Johns Hopkins APL Technical Digest 24, 156–164.